Layered mixed tin-lead hybrid perovskite solar cells with high stability

Daniel Ramirez,[a] Kelly Schutt,[b] Zhiping Wang,[b] Andrew J. Pearson,[c] Edoardo Ruggeri,[c] Henry J. Snaith,[b] Samuel D. Stranks,[c] and Franklin Jaramillo[a*]

a. Centro de Investigación, Innovación y Desarrollo de Materiales – CIDEMAT, Facultad de Ingeniería, Universidad de Antioquia UdeA, Calle 70 No. 52-21, Medellín, Colombia.

b. Department of Physics, University of Oxford, Clarendon Laboratory, Parks Road, Oxford, OX13PU, United Kingdom.

c. Cavendish Laboratory, Department of Physics, University of Cambridge, JJ Thomson Avenue, Cambridge CB3 0HE, UK

Abstract

Tin-lead mixed metal hybrid perovskites with tunable band gaps are attractive candidates to be used as the low-band gap cell in high efficiency tandem solar cells. Nevertheless, perovskites containing tin have a greater propensity to degrade due to the fast oxidation of Sn^{2+} to Sn^{4+}, which is a restrictive factor in the development of these materials. Although significant improvements are achieved with Pb:Sn mixed-metal perovskites, in comparison to neat Sn perovskites, the intrinsic instability may still pose a threat to long-term operation. For neat Pb perovskites, two dimensional (2D) hybrid perovskites, where n layers of inorganic material are separated by a long chain organic cation, generally exhibit greater stability but have lower photovoltaic performance characteristics, motivating the study of 2D/3D mixed dimension systems to realize both high efficiency and stability. In this report we demonstrate such optimal performance and stability using formamidinium, cesium and t-butylammonium as A-site cations with Pb:Sn mixed metal low band gap perovskites. As determined by film structure measurements, the optimised 2D perovskite phases facilitate improved luminescence efficiency, which we infer to be via surface defect site passivation. Perovskite solar cells based on n = 4 and n = 5 lead-tin perovskites achieved power conversion efficiencies of up to 9.3% and 10.6%, respectively and correspondingly retained 47% and 29% of their initial efficiency during storage in nitrogen for 2000 hours. A similar stability trend for n = 4 over n = 5 was also observed for unencapsulated devices during continuous operation under combined air atmosphere and temperature for 10 hours, resulting in improved stability over the 3D lead-tin counterpart.

Hybrid organic-inorganic perovskites have been extensively developed in the past few years due to their outstanding semiconductor properties including large absorption coefficient, [1,2] tunable band gap,[2] and long exciton and charge-carrier diffusion lengths.[3] As a consequence, impressive results in different fields such as solar cells,[4–6] light emitting diodes (LEDs)[7] and photodetectors[8] have been obtained. Specifically, in the field of solar cells, hybrid organic-inorganic perovskite solar cells (PSCs) have become one of the most attractive forms of this technology as a result of rapid improvements in champion power conversion efficiency (PCE), from 3.8 % in 2009 to 22.7 % last year.[9,10] This value has been achieved through intensive research and development of 1.6 eV bandgap lead-based perovskite absorbers.[11–13] Realising the full potential of these hybrid materials relies also upon the ability to modulate their band gap by modifying the B site cation, typically

lead, in the three dimensional (3D) ABX_3 perovskite structure. If the lead cation is completely replaced by tin, then a narrower band gap of 1.4 eV can be obtained; while if it is partially replaced, band gaps as low as 1.2 eV can be obtained.[14,15] This has motivated researchers in the field of tandem solar cells,[16] because a double junction tandem PSC can potentially yield up to 36% power conversion efficiency (PCE).[17] Particularly, perovskite tandem solar cells have been obtained using $FA_{0.83}Cs_{0.17}Pb(I_{0.5}Br_{0.5})_3$ and $FA_{0.75}Cs_{0.25}Sn_{0.5}Pb_{0.5}I_3$ as wide and narrow band gap absorbers, respectively. These tandem devices achieved PCEs of 17.0% and 20.3% in monolithic two terminal and mechanically stacked four terminal tandem solar cells, respectively.[18] Recently, the highest PCE in four terminal configuration is 23.1% by using $FA_{0.8}Cs_{0.2}Pb(I_{0.7}Br_{0.3})_3$ and $(FASnI_3)_{0.6}(MAPbI_3)_{0.4}$.[19]

However, the sensitivity of the Sn-based perovskites to fast oxidation, where Sn^{2+} transforms to Sn^{4+}, is a restrictive factor in the development of these semiconductors for stable PSCs.[20] Mixed tin-lead perovskites also exhibit poor intrinsic stability, with a degradation mechanism dependent not only in the tin content but also in the A site cation.[21] In general, one of the most successful attempts to improve the stability of both tin and lead-based perovskite is the partial substitution of the A site cation for a larger hydrophobic cation that reduces both oxygen and moisture ingress.[22] This substitution leads to a two dimensional (2D) hybrid perovskite structure that can be stoichiometrically described by the formula $A_2A'_{n-1}B_nX_{3n+1}$ where A, A' are cations, B is metal and X is halide. The resulting material in then referred as a Ruddlesden-Popper perovskite with lower dimensionality as the number of inorganic layers separated by the hydrophobic cation (*n*) goes from infinity to one.[23] To date the highest PCE for the 2D Ruddlesden-Popper perovskites is 13.7% in a lead-based composition with Cs doping.[24] For the case of tin, PSCs with PCE of 5.94% have been demonstrated by introducing a small amount of a larger phenylethylammonium (PEA) cation to form a mixed two dimensional 2D/3D absorber.[25] This value was recently improved by optimizing the material composition, leading to better stability and a PCE of 9.0%.[26] The most promising A' cations are those containing only a few carbon atoms that can provide stability without negatively impacting the device performace, as is the case for the larger A' cations such as PEA. The most widely studied molecules containing 4 carbon atoms are n-butylammonium (n-BA),[22,27] iso-butylammonium (i-BA)[28] and tetra-butylammonium (tetra-BA),[29] but there is also tert-butylammonium (t-BA) with shorter axial chain length and higher thermal stability than the other molecules. In this work we incorporate t-BA as A' cation in combination with formamidinium (FA) and cesium (Cs) in the mixed Sn/Pb low band gap perovskite system. We observed that this cation is able to form a passivating 2D perovskite structure, leading to device performance up to 10.6% and improved stability under continuous operation with air, simulated sunlight and temperature exposure when compared to the 3D counterpart.

A primary goal of Sn perovskites is to achieve low band gap materials, and it has been demonstrated that narrower (than the singles metal counterparts) band gaps are obtained in the mixed Sn/Pb systems, with common ratios of Sn/Pb from 0.67 to 1.5.[14] Using Pb/Sn=1.5 as metal cations (less Sn to have better stability), iodine as anion and t-BA, FA and Cs as cations, we fabricated $(t\text{-}BA)_2(FA_{0.85}Cs_{0.15})_{n-1}(Pb_{0.6}Sn_{0.4})_nI_{3n+1}$ films when the *n* value is modified from *n=2 to n=9*. We note that we first optimized the FA/Cs ratio for both morphology and performance, as explained in the supplementary information (Figure S1). Figure 1a-d shows the change in morphology of the films for the optimal FA/Cs ratios when increasing dimensionality from *n=2* to

n=5, with increasing grain size over these values followed by a reduction for *n=9*. All compositions presented well-defined grains with some plate-like morphology embedded at the grain boundaries. This plate-like morphology could correspond to some segregated 2D perovskite or to some impurities. However, these plate-like structures were absent in films annealed at lower temperatures (100 °C and 130 °C), which also resulted in smaller grains of size ~40 nm, similar to those reported for other 2D perovskites[27] (Figure S2); without any reflections at low angles according to the XRD data (Figure S3), suggesting that the plate-like structures could be a new phase, which we will discuss later.

In Figure 1e and 1f, we show the absorption profiles and photoluminescence (PL) spectra of the films, respectively. The absorption onset and emission peak are shifted to higher wavelengths when the *n* value is increased. The spectral shift between the absorption onset and emission peak is only a few meV, and unlikely to be due to the emission emerging from a lower dimensionality phase,[30] allowing us to calculate a bulk band gap of c.a. 1.24 eV for n>2 as shown in the inset of Figure 1e (see Tauc plots used to calculate the band gap in Figure S4). We observe an increasing PL intensity (Figure 1f) and lifetime (Figure 1g) from n=2 up to a peak of n=5 (being almost identical to n=3 and with a time taken to fall to half of initial intensity, $\tau_{1/2}$= 6.7 ns), with the intensity and lifetime then dropping for n=9 ($\tau_{1/2}$= 5.1 ns). This indicates that the n=5 system exhibits the ideal combined characteristics of large grain size for the 3D phase and segregated 2D phases that appear to passivate trap states in lead-based perovskites incoprating the BA cation.[31]

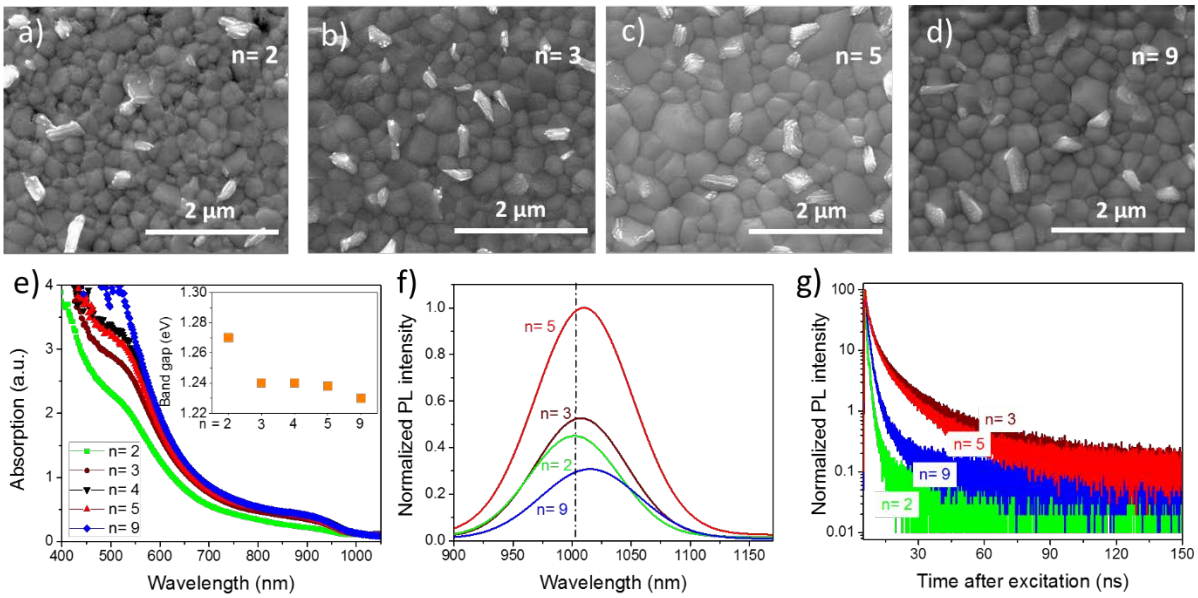

Figure 1: Characterisation of $(t\text{-BA})_2(FA_{0.85}Cs_{0.15})_{n-1}(Pb_{0.6}Sn_{0.4})_nI_{3n+1}$ thin films. SEM images for a) n=2, b) n=3, c) n=5 and d) n=9. Scale bar corresponds to 2µm. e) Absorption spectra with the inset showing the calculated band gap from Tauc plots, f) steady state PL and g) TRPL of films excited at 634 nm for n=2, 3, 5, and 9. The TRPL measurements were acquired at a fluence of 0.2 µJ/cm^2/pulse.

The X-ray diffraction (XRD) patterns (Figure 2a) show strong diffraction peaks at around 2θ = 14.0° and 28°, which correspond to the (100) and (200) reflections from a typical 3D perovskite cubic phase.[14,32] Additionally, we also observed multiple low angle peaks at 2θ = 8.7°, 10.3° and 10.8°.

These reflections are too low in 2θ to correspond to 3D perovskites. Considering that perovskites incorporating the long ammonium BA cation usually show 2D layered structure,[22,31] we therefore attribute these low angle reflections to originate from 2D perovskite phases. The observed non-related multiplicity of these peaks suggests that a mixture of different n-values was obtained; therefore each sample is not a strict binary phase system. We also observed that, as expected, the peak intensities of the 2D phases reduced as the n-value increased, and that the high excess of PbI_2 in n=9 sample (2θ = 12.6˚) may promote disorder due to defects and vacancies, which could be one of the causes of the sample's low PL intensity and recombination lifetime.

To obtain a deeper understanding of each sample's morphology we performed grazing-incidence wide-angle X-ray scattering (GIWAXS) measurements, which provides information on sample surface structure and the grain orientation distribution of different crystalline phases. We show GIWAXS patterns in Figure 2b and 2c for n=3 and n=5 respectively, where we observe powder diffraction rings indicating the polycrystalline nature of both the 3D and 2D perovskite grains. Note that unlike bulk XRD, GIWAXS can reveal diffraction planes within the film that are non-normal to the substrate, such as slantwise planes or planes that display preferred perpendicular orientation of the periodicity of the 2D perovskite slabs.[25] In our case we did not observe preferred orientation, but the isotropic rings found at 0.62 Å, 0.73 Å and 0.77 Å are consistent with the previous XRD data. The reduced 1D GIWAXS patterns are shown in Figure 2d and provide clearer evidence for the existence of 2D phases that are randomly oriented throughout the film.

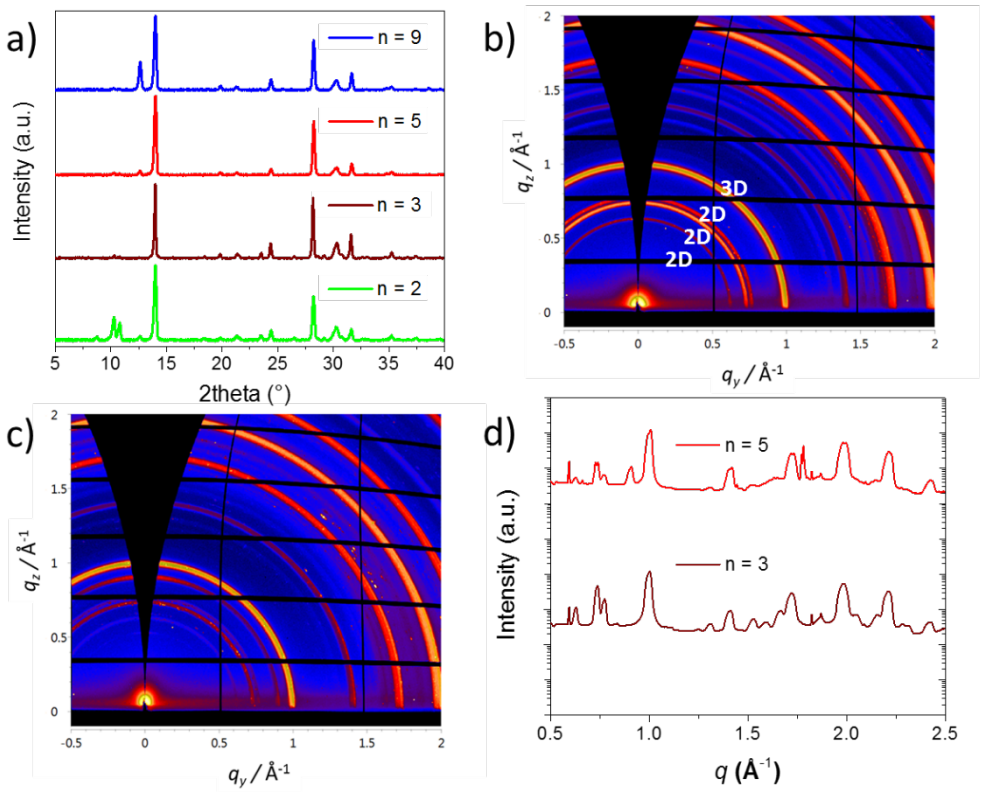

Figure 2: Structural characterization of $(t\text{-}BA)_2(FA_{0.85}Cs_{0.15})_{n-1}(Pb_{0.6}Sn_{0.4})_nI_{3n+1}$ thin films. a) XRD patterns and 2D GIWAXS patterns for b) n=3 and c) n=5 and d) reduced 1D GIWAXS patterns along q_z.

In order to validate their performance in solar cells, we fabricated planar heterojunction solar cells with the architecture ITO/PEDOT:PSS/$(t\text{-}BA)_2(FA_{0.85}Cs_{0.15})_{n-1}(Pb_{0.6}Sn_{0.4})_nI_{3n+1}$/PCBM/BCP/Ag. In Figure 3a, we show current density-voltage (J-V) data for the solar cells, with the corresponding performance metrics presented in Table 1. The best performing device was obtained for n=5, which exhibited a J_{sc} of 24.2 mA/cm^2, a V_{oc} of 0.70, and a FF of 0.63, yielding a PCE of 10.6% reduced hysteresis as indicated. We note that the devices exhibited hysteresis in the forward and backward scans (see SI Figure S5) but this was reduced for n=5; this can also be seen in the reduced data dispersion in Figure 3b which includes both forward and reverse scanning direction data. Box plots of all other photovoltaic parameters are shown in Figure S6. By increasing n from 2 to 5, we observed significant improvements in J_{sc}, which is consistent with a reduced transport efficiency when a large amount of 2D material is present (as for n= 2).[33]

In order to understand the stabilized operation, we acquired the stabilized power output (SPO) by measuring the current at a fixed maximum power point (MPP) voltage over 50 s, which we show in Figure 3c. We find that for the n=5 PSC a champion SPO of 9.6% can be obtained, compared to SPOs of 8.4% and 4.4% for n=4 and n=2, respectively. Finally, the calculated external quantum efficiency (EQE) of the devices is shown in Figure 3d, indicating that each of the compositions studied can generate a photocurrent following absorption of light from the near Infrared (NIR) region. The EQE onset also showed a displacement towards shorter wavelengths for n=2 containing more t-BA cation and is in agreement with the previous calculated band gaps; in this case, the small onset displacement combined with lower response across all wavelengths in the EQE for the n=2 cell is in part responsible for the lower J_{sc}. We also find that the FA/Cs ratios shown here yield the highest performance (Figure S7 and Table S1).

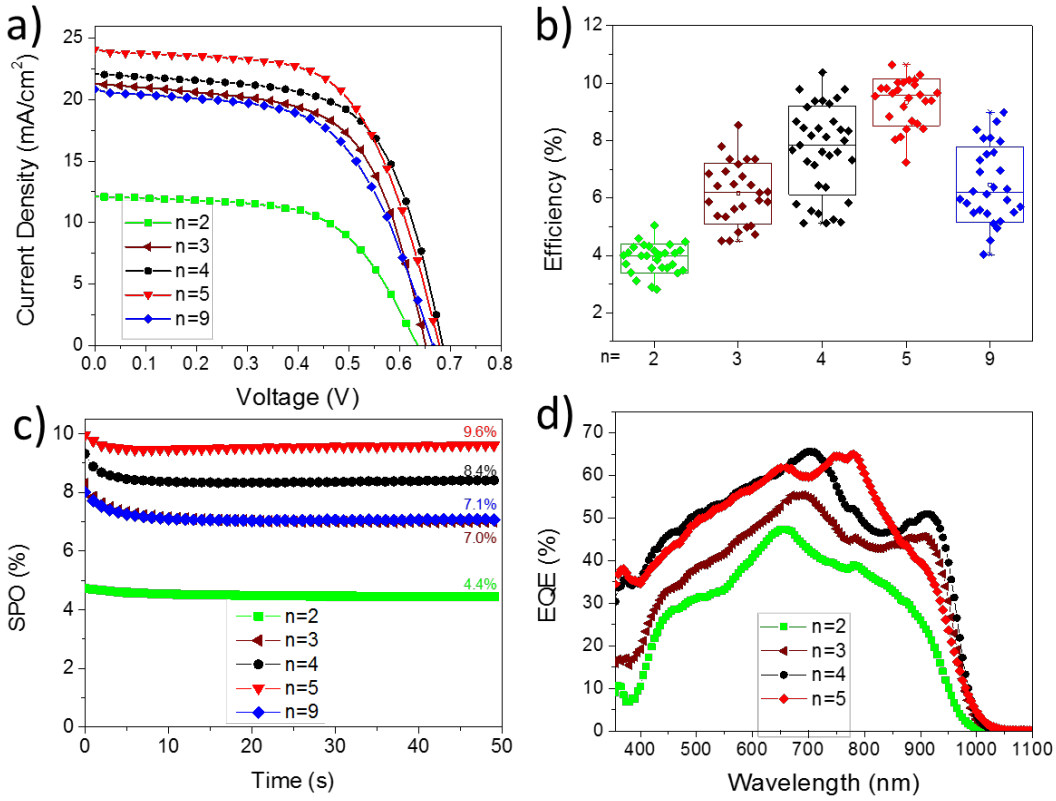

Figure 3: Photovoltaic performance of n-value dependent solar cells using $(t\text{-}BA)_2(FA_{0.85}Cs_{0.15})_{n-1}(Pb_{0.6}Sn_{0.4})_nI_{3n+1}$ as active layer. a) JV curves, b) power conversion efficiency (PCE) box plot, c) SPO and d) EQE. PCE was measured under AM1.5 100 mW/cm^2.

Table 2. *n-value dependent* solar cell performance parameters for $(t\text{-}BA)_2(FA_{0.85}Cs_{0.15})_{n-1}(Pb_{0.6}Sn_{0.4})_nI_{3n+1}$ solar cells determined from *J–V* curves in Figure 3.

Device	PCE (%)	J_{sc} (mA/cm^2)	V_{oc} (V)	FF
n = 2				
Average	3.9±0.5	12.2±0.6	0.59±0.03	0.54±0.04
Champion	5.0	13.9	0.61	0.59
n = 3				
Average	6.3±1.0	18.3±1.6	0.62±0.03	0.55±0.04
Champion	8.5	21.3	0.64	0.60
n = 4				
Average	7.6±1.5	20.8±1.8	0.64±0.04	0.57±0.06
Champion	10.4	24.2	0.70	0.61
n = 5				
Average	9.3±0.8	23.9±0.6	0.66±0.02	0.59±0.04
Champion	10.6	24.2	0.70	0.63
n = 9				
Average	6.4±1.3	19.6±2.1	0.61±0.05	0.54±0.06
Champion	8.9	23.5	0.67	0.57

To assess the stability of the PSCs we tracked the changes in SPO for unencapsulated devices over 2000 hours with glovebox storage (N_2 atmosphere) between measurements. As shown in Figure 4a, the n=2 and n=3 devices exhibit a faster decay, which could be related to defect-induced degradation,[34] because even though they had the higher 2D content, for instance, n=2 had poorer film quality with evident pinholes (Figure 1a) and lower radiative efficiency. Note that similar to the lead-based 2D/3D perovskites J_{sc} was the most affected parameter,[31] as shown in Figure S8. In contrast, the highest efficiency PSCs, n=4 and n=5, were also the most stable, retaining 47% and 29% of their initial SPOs after 2000 hours, respectively. Resulting in the longest stability test for mixed tin-lead perovskites.

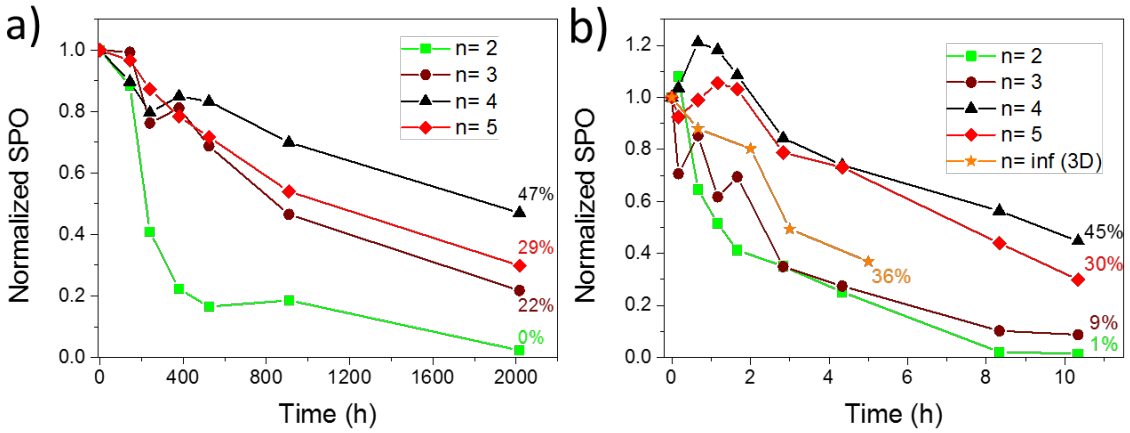

Figure 4: Evolution of the normalized SPO over time for unencapsulated devices stored a) under nitrogen atmosphere and b) exposed continuously to 1 sun illumination and 65 °C temperature under ambient air atmosphere.

We also monitored the stability of these PSCs aged under air, 1 sun illumination and 65 °C. Figure 4b shows a faster decay for n=2 and n=3, which rapidly reduced the SPO to less than 1% after 8.3 h, which we propose is due to the combined self-defect and external- (air-) induced degradation. The n= 4 and n= 5 devices showed better stability, with n= 4 retaining 45% of its initial value after 10 hours. Interestingly, in both cases, there was a rise in efficiency in the first hour before the onset of the degradation. This may be due to the same photo-induced trap passivation observed in Pb based perovskites, resulting in initial improvements before degradation sets in.[35] It may also be due to the self-doping which occurs due to Sn vacancy generation in the Sn^{2+} to Sn^{4+} degradation process,[25] where "optimum doping" may occur after a certain period of degradation. To compare this with a 3D mixed Sn/Pb perovskite we also fabricated the devices (Photovoltaic performance shown in Figure S9), and we observe that SPO went down to 36% of its initial value after 5h, corroborating the improved stability of our t-BA based 2D perovskites.

Conclusions

In conclusion, we investigated the formation and device performance of the 2D low band gap (~1.24 eV) mixed tin-lead hybrid perovskite system, by introducing t-BA molecules to form 2D

domains within the FA/Cs 3D perovskite. The 2D domains increasing the PL efficiency and lifetime by passivating non-radiative decay pathways. Diffraction studies reveal that the passivating 2D domains are randomly distributed throughout the film. The resulting hybrid perovskites with 10.6% efficiency showed improved device stability, making them attractive candidates for high efficiency low cost tandem solar cells. Our results demonstrate that achieving stable operation mixed tin-lead hybrid perovskites is possible and therefore, future investigations in this direction are highly encouraged.

Methods

$(t\text{-}BA)_2(FA_{(1-x)}\ Cs_x)_2(Pb_{0.6}Sn_{0.4})_3I_{10}$ and $(t\text{-}BA)_2(FA_{0.85}Cs_{0.15})_{n-1}(Pb_{0.6}Sn_{0.4})_nI_{3n+1}$ precursor solutions.

The *$(t\text{-}BA)_2(FA_{(1-x)}\ Cs_x)_2(Pb_{0.6}Sn_{0.4})_3I_{10}$* precursor solution was prepared by mixing Formamidinium iodide (FAI) (Dyesol), cesium iodide (CsI) (Alfa Aesar, 99.99%), lead iodide (PbI_2) (TCI, 99.999%) tin iodide (SnI_2) (Sigma-Aldrich, Anhydrous, 99.99%) and tin fluoride (SnF_2) with a molar ratio of 2:2(1-x):2x:1.8:1.2:0.24 = t-BU:FAI:CsI:PbI_2:SnI_2:SnF_2. Note that the 0.24 moles of SnF_2 corresponds to a 20% excess respect to SnI_2, in order to prevent solution oxidation. The mixed powders were dissolved in anhydrous N,N-dimethylformamide (DMF) (Sigma-Aldrich, 99.8%) to give a 69 %w/v solution when x=0. The solutions were stirred overnight in a nitrogen-filled glove box, prior use.

$(t\text{-}BA)_2(FA_{0.85}Cs_{0.15})_{n-1}(Pb_{0.6}Sn_{0.4})_nI_{3n+1}$ precursor solution was prepared the same solution concentration was used, but as the FA/Cs ration was kept fixed to 85/15, then the powders mixing was modulated according to the molar ratio of 2:0.85(n-1):0.15(n-1):0.6n:0.4n = t-BU:FAI:CsI:PbI_2:SnI_2. 20% excess of SnF_2 respect to SnI_2 was also added to all solution. These solutions were also stirred overnight in a nitrogen-filled glove box, prior use.

t-BA/FA/Cs Solar cell fabrication

ITO substrates were sonicated in water (5 min), Acetone (5 min) and Isopropanol (IPA) (5 min), then dried and O_2-plasma treated (10 min). PEDOT:PSS (Clevios, P VP AI 4083) was diluted 2:1 by volume (methanol: PEDOT:PSS) and then spin coated in a drybox at 4000rpm, with a 4000rpm/s ramp during 40s. The substrates were then annealed at 150 °C for 10 min and then transferred to a glove box, where they were annealed again at 120 °C for 10 min before depositing the perovskite. All the perovskite precursor solutions were deposited using a two-step program, 1000 rpm and 4000 rpm for 10 and 15 s, respectively. 18 s after the program started, 200 µL of anhydrous toluene (Sigma-Aldrich, 99%) was dropped, forming immediately a dark brown perovskite film. The substrates were then annealed at 100 °C, 130 °C or 150 °C for 20 minutes. Filtered PCBM solution (20 mg/mL in 3:1 by volume Chlorobenzene:(1,2-Dichlorobenzene)) was deposited by dynamic spin coating at 2000 rpm during 30 s. The substrates where then place on a hotplate at 80 °C for 5 minutes. Then a solution of 0.5mg BCP in 1ml of IPA was deposited at 4000 rpm. Finally, to complete the devices, 100 nm silver electrode was thermally evaporated.

3D $(FA_{0.85}Cs_{0.15})(Pb_{0.6}Sn_{0.4})I_3$ Solar cell fabrication

The same procedure as for the t-BA/FA/Cs solar cell was followed. But in this case the precursor solution did not contain t-BA. A mixture of DMF:DMSO (4:1 volume) instead of only DMF was used, because the films containing only DMF formed cracks after toluene was dropped.

Current-voltage measurements

Solar cells were measured with an Abet Class AAB solar simulator under simulated AM 1.5 sunlight at 100 mW cm^{-2} irradiance, calibrated by an NREL-calibrated KG5 filtered silicon reference cell. The mismatch factor was calculated at < 1%. J-V curves were recorded with a 2400 Series Sourcemeter by Keithly Instruments. The solar cell active area was 0.0919 cm^{-2}.

External quantum efficiency (EQE)

EQE spectra were evaluated via custom-built Fourier transform photocurrent spectroscopy based on the Bruker Vertex 80v Fourier transform spectrometer. A Newport AAA sun simulator was used as the light source and the light intensity was calibrated with a Newport-calibrated reference silicon photodiode

Ultraviolet-visible absorption (Uv-vis)

The steady-state absorption spectra were acquired with a Perkin-Elmer Lambda 1050 UV/Vis/NIR spectrophotometer.

Photoluminescence spectroscopy

Steady-state and time-resolved PL measurements were performed using a time resolved single-photon counting setup (FluoTime 300, PicoQuant GmbH) using a 634 nm pulsed laser as excitation at frequencies between 2 MHz and 5MHz.

Scanning electron microscopy (SEM)

The morphology of perovskite films was investigated using a SEM (Hitachi S-4300)

X-ray diffraction (XRD)

For the Mixed tin-lead perovskites a Rigaku SmartLab X-ray diffractometer with Cu Kα radiation was used.

GIWAXS

Samples were measured in a grazing-incidence geometry at beamline I07 of the Diamond Light Source (Harwell, UK). A beam energy of 10 keV was used with samples housed in a custom-built chamber during measurement. Samples were tilted at 0.3° into the path of the incident X-rays. X-ray scatter was measured using a Pilatus 2M detector, calibrated using silver behenate powder. Collected data were analyzed using the DAWN software package (http://www.dawnsci.org/).

Stability test

Unencapsulated devices were kept inside a nitrogen-filled glovebox over 910 h for the operational performance test. These devices were air exposed for around 10 min during photovoltaic characterization. Other set of unencapsulated devices were aged under open-circuit conditions,

under full-spectrum simulated AM1.5, 76mA/cm^2 irradiance, using an Atlas SUNTEST XLS+ (1,700W air-cooled xenon lamp). We note that the light source is pulsed at 100Hz frequency and we do not apply any additional ultraviolet filter during the ageing process. The chamber is air-cooled to have a temperature around 60 °C as indicated by a black standard temperature control unit mounted inside. We do not have control on the humidity but monitored the laboratory humidity, which around 50% relative humidity at room temperature, during the course of the ageing.

Acknowledgements

We thank the Colombian "Departamento Nacional de Planeación", SGR collaborative project 2013000100184 between Empresas Públicas de Medellin, Andercol S.A., Sumicol S.A.S., Universidad de Antioquia. K. S. is supported by Marshall Aid Commemoration Commission. This work was part funded by EPSRC UK. This project has received funding from the European Research Council (ERC) under the European Union's Horizon 2020 research and innovation programme (grant agreement number 756962). E.R. was partially supported by an EPSRC Departmental Graduate Studentship. S.D.S acknowledges support from the Royal Society and Tata Group (UF150033). This work was carried out with the support of the Diamond Light Source (proposal SI17223-1)

References

(1) Wenger, B.; Nayak, P. K.; Wen, X.; Kesava, S. V.; Noel, N. K.; Snaith, H. J. Consolidation of the optoelectronic properties of CH3NH3PbBr3 perovskite single crystals. *Nat. Commun.* **2017**, *8* (1), 590 DOI: 10.1038/s41467-017-00567-8.

(2) Jung, H. S. H. S.; Park, N.-G. N.-G. Perovskite Solar Cells: From Materials to Devices. *Small* **2015**, *11* (1), 10–25 DOI: 10.1002/smll.201402767.

(3) Stranks, S. D.; Eperon, G. E.; Grancini, G.; Menelaou, C.; Alcocer, M. J. P.; Leijtens, T.; Herz, L. M.; Petrozza, A.; Snaith, H. J. Electron-hole diffusion lengths exceeding 1 micrometer in an organometal trihalide perovskite absorber. *Science* **2013**, *342* (6156), 341–344 DOI: 10.1126/science.1243982.

(4) Bi, D.; Tress, W.; Dar, M. I.; Gao, P.; Luo, J.; Renevier, C.; Schenk, K.; Abate, A.; Giordano, F.; Correa Baena, J.-P.; et al. Efficient luminescent solar cells based on tailored mixed-cation perovskites. *Sci. Adv.* **2016**, *2* (1), e1501170–e1501170.

(5) Mali, S. S.; Shim, C. S.; Hong, C. K. Highly stable and efficient solid-state solar cells based on methylammonium lead bromide (CH3NH3PbBr3) perovskite quantum dots. *NPG Asia Mater.* **2015**, *7* (8), e208 DOI: 10.1038/am.2015.86.

(6) Giesbrecht, N.; Schlipf, J.; Oesinghaus, L.; Binek, A.; Bein, T.; Müller-Buschbaum, P.; Docampo, P. Synthesis of Perfectly Oriented and Micrometer-Sized MAPbBr $_3$ Perovskite Crystals for Thin-Film Photovoltaic Applications. *ACS Energy Lett.* **2016**, *1* (1), 150–154 DOI: 10.1021/acsenergylett.6b00050.

(7) Li, G.; Tan, Z.-K.; Di, D.; Lai, M. L.; Jiang, L.; Lim, J. H.-W.; Friend, R. H.; Greenham, N. C.

Efficient light-emitting diodes based on nanocrystalline perovskite in a dielectric polymer matrix. *Nano Lett.* **2015**, *15* (4), 2640–2644 DOI: 10.1021/acs.nanolett.5b00235.

(8) Ahmadi, M.; Wu, T.; Hu, B. A Review on Organic-Inorganic Halide Perovskite Photodetectors: Device Engineering and Fundamental Physics. *Adv. Mater.* **2017**, *29* (41), 1605242 DOI: 10.1002/adma.201605242.

(9) Kojima, A.; Teshima, K.; Shirai, Y.; Miyasaka, T. Organometal Halide Perovskites as Visible-Light Sensitizers for Photovoltaic Cells. *J. Am. Chem. Soc.* **2009**, *131* (17), 6050–6051 DOI: 10.1021/ja809598r.

(10) NREL. Best Research-Cell Efficiencies http://www.nrel.gov/ncpv/images/efficiency_chart.jpg.

(11) Yang, W. S.; Park, B.-W.; Jung, E. H.; Jeon, N. J.; Kim, Y. C.; Lee, D. U.; Shin, S. S.; Seo, J.; Kim, E. K.; Noh, J. H.; et al. Iodide management in formamidinium-lead-halide-based perovskite layers for efficient solar cells. *Science* **2017**, *356* (6345), 1376–1379 DOI: 10.1126/science.aan2301.

(12) Hou, Y.; Zhang, H.; Chen, W.; Chen, S.; Quiroz, C. O. R.; Azimi, H.; Osvet, A.; Matt, G. J.; Zeira, E.; Seuring, J.; et al. Inverted, Environmentally Stable Perovskite Solar Cell with a Novel Low-Cost and Water-Free PEDOT Hole-Extraction Layer. *Adv. Energy Mater.* **2015**, *5* (15), 1500543 DOI: 10.1002/aenm.201500543.

(13) Li, X.; Bi, D.; Yi, C.; Decoppet, J.-D.; Luo, J.; Zakeeruddin, S. M.; Hagfeldt, A.; Gratzel, M. A vacuum flash-assisted solution process for high-efficiency large-area perovskite solar cells. *Science (80-.).* **2016**, *353* (6294), 58–62 DOI: 10.1126/science.aaf8060.

(14) Prasanna, R.; Gold-Parker, A.; Leijtens, T.; Conings, B.; Babayigit, A.; Boyen, H.-G.; Toney, M. F.; McGehee, M. D. Band Gap Tuning via Lattice Contraction and Octahedral Tilting in Perovskite Materials for Photovoltaics. *J. Am. Chem. Soc.* **2017**, *139* (32), 11117–11124 DOI: 10.1021/jacs.7b04981.

(15) Song, T.-B.; Yokoyama, T.; Aramaki, S.; Kanatzidis, M. G. Performance Enhancement of Lead-Free Tin-Based Perovskite Solar Cells with Reducing Atmosphere-Assisted Dispersible Additive. *ACS Energy Lett.* **2017**, *2* (4), 897–903 DOI: 10.1021/acsenergylett.7b00171.

(16) Eperon, G. E.; Hörantner, M. T.; Snaith, H. J. Metal halide perovskite tandem and multiple-junction photovoltaics. *Nat. Rev. Chem.* **2017**, *1* (12), 0095 DOI: 10.1038/s41570-017-0095.

(17) Rajagopal, A.; Yang, Z.; Byeok Jo, S.; Braly, I. L.; Liang, P.-W.; Hillhouse, H. W.; K-Y Jen, A.; Rajagopal, A.; Yang, Z.; Jo, S. B.; et al. Highly Efficient Perovskite–Perovskite Tandem Solar Cells Reaching 80% of the Theoretical Limit in Photovoltage. *Adv. Mater.* **2017**, *29* (34), 1702140 DOI: 10.1002/adma.201702140.

(18) Eperon, G. E.; Leijtens, T.; Bush, K. A.; Prasanna, R.; Green, T.; Wang, J. T.-W.; McMeekin, D. P.; Volonakis, G.; Milot, R. L.; May, R.; et al. Perovskite-perovskite tandem photovoltaics with optimized band gaps. *Science* **2016**, *354* (6314), 861–865 DOI: 10.1126/science.aaf9717.

(19) Zhao, D.; Wang, C.; Song, Z.; Yu, Y.; Chen, C.; Zhao, X.; Zhu, K.; Yan, Y. Four-Terminal All-Perovskite Tandem Solar Cells Achieving Power Conversion Efficiencies Exceeding 23%. *ACS Energy Lett.* **2018**, *3* (2), 305–306 DOI: 10.1021/acsenergylett.7b01287.

(20) Liao, W.; Zhao, D.; Yu, Y.; Shrestha, N.; Ghimire, K.; Grice, C. R.; Wang, C.; Xiao, Y.; Cimaroli, A. J.; Ellingson, R. J.; et al. Fabrication of Efficient Low-Bandgap Perovskite Solar Cells by Combining Formamidinium Tin Iodide with Methylammonium Lead Iodide. *J. Am. Chem. Soc.* **2016**, *138* (38), 12360–12363 DOI: 10.1021/jacs.6b08337.

(21) Leijtens, T.; Prasanna, R.; Gold-Parker, A.; Toney, M. F.; McGehee, M. D. Mechanism of Tin Oxidation and Stabilization by Lead Substitution in Tin Halide Perovskites. *ACS Energy Lett.* **2017**, *2* (9), 2159–2165 DOI: 10.1021/acsenergylett.7b00636.

(22) Cao, D. H.; Stoumpos, C. C.; Farha, O. K.; Hupp, J. T.; Kanatzidis, M. G. Two-dimensional homologous perovskites as light absorbing materials for solar cell applications. *J. Am. Chem. Soc.* **2015**, *137* (24), 7843–7850.

(23) Stoumpos, C. C.; Cao, D. H.; Clark, D. J.; Young, J.; Rondinelli, J. M.; Jang, J. I.; Hupp, J. T.; Kanatzidis, M. G. Ruddlesden–Popper Hybrid Lead Iodide Perovskite 2D Homologous Semiconductors. *Chem. Mater.* **2016**, *28* (8), 2852–2867 DOI: 10.1021/acs.chemmater.6b00847.

(24) Zhang, X.; Ren, X.; Liu, B.; Munir, R.; Zhu, X.; Yang, D.; Li, J.; Liu, Y.; Smilgies, D.-M.; Li, R.; et al. Stable high efficiency two-dimensional perovskite solar cells via cesium doping. *Energy Environ. Sci.* **2017**, *10* (10), 2095–2102 DOI: 10.1039/C7EE01145H.

(25) Liao, Y.; Liu, H.; Zhou, W.; Yang, D.; Shang, Y.; Shi, Z.; Li, B.; Jiang, X.; Zhang, L.; Quan, L. N.; et al. Highly Oriented Low-Dimensional Tin Halide Perovskites with Enhanced Stability and Photovoltaic Performance. *J. Am. Chem. Soc.* **2017**, *139* (19), 6693–6699 DOI: 10.1021/jacs.7b01815.

(26) Shao, S.; Liu, J.; Portale, G.; Fang, H.-H.; Blake, G. R.; ten Brink, G. H.; Koster, L. J. A.; Loi, M. A. Highly Reproducible Sn-Based Hybrid Perovskite Solar Cells with 9% Efficiency. *Adv. Energy Mater.* **2018**, *8*, 1702019 DOI: 10.1002/aenm.201702019.

(27) Tsai, H.; Nie, W.; Blancon, J.-C.; Stoumpos, C. C.; Asadpour, R.; Harutyunyan, B.; Neukirch, A. J.; Verduzco, R.; Crochet, J. J.; Tretiak, S.; et al. High-efficiency two-dimensional Ruddlesden–Popper perovskite solar cells. *Nature* **2016**, *536*, 312–316 DOI: 10.1038/nature18306.

(28) Chen, Y.; Sun, Y.; Peng, J.; Zhang, W.; Su, X.; Zheng, K.; Pullerits, T.; Liang, Z. Tailoring Organic Cation of 2D Air-Stable Organometal Halide Perovskites for Highly Efficient Planar Solar Cells. *Adv. Energy Mater.* **2017**, *7* (18), 1700162 DOI: 10.1002/aenm.201700162.

(29) Poli, I.; Eslava, S.; Cameron, P. Tetrabutylammonium cations for moisture-resistant and semitransparent perovskite solar cells. *J. Mater. Chem. A* **2017**, *5* (42), 22325–22333 DOI: 10.1039/C7TA06735F.

(30) Milot, R. L.; Sutton, R. J.; Eperon, G. E.; Haghighirad, A. A.; Martinez Hardigree, J.; Miranda, L.; Snaith, H. J.; Johnston, M. B.; Herz, L. M. Charge-Carrier Dynamics in 2D Hybrid Metal–Halide Perovskites. *Nano Lett.* **2016**, *16* (11), 7001–7007 DOI: 10.1021/acs.nanolett.6b03114.

(31) Wang, Z.; Lin, Q.; Chmiel, F. P.; Sakai, N.; Herz, L. M.; Snaith, H. J. Efficient ambient-air-stable solar cells with 2D–3D heterostructured butylammonium-caesium-formamidinium lead halide perovskites. *Nat. Energy* **2017**, *2* (9), 17135 DOI: 10.1038/nenergy.2017.135.

(32) Liu, C.; Fan, J.; Li, H.; Zhang, C.; Mai, Y. Highly Efficient Perovskite Solar Cells with Substantial Reduction of Lead Content. *Sci. Rep.* **2016**, *6* (1), 35705 DOI: 10.1038/srep35705.

(33) Blancon, J.-C.; Tsai, H.; Nie, W.; Stoumpos, C. C.; Pedesseau, L.; Katan, C.; Kepenekian, M.; Soe, C. M. M.; Appavoo, K.; Sfeir, M. Y.; et al. Extremely efficient internal exciton dissociation through edge states in layered 2D perovskites. *Science* **2017**, *355* (6331), 1288–1292 DOI: 10.1126/science.aal4211.

(34) Khadka, D. B.; Shirai, Y.; Yanagida, M.; Miyano, K. Degradation of encapsulated perovskite solar cells driven by deep trap states and interfacial deterioration. *J. Mater. Chem. C* **2018**, *6* (1), 162–170 DOI: 10.1039/C7TC03733C.

(35) deQuilettes, D. W.; Zhang, W.; Burlakov, V. M.; Graham, D. J.; Leijtens, T.; Osherov, A.; Bulović, V.; Snaith, H. J.; Ginger, D. S.; Stranks, S. D. Photo-induced halide redistribution in organic–inorganic perovskite films. *Nat. Commun.* **2016**, *7*, 11683 DOI: 10.1038/ncomms11683.